ORIGINAL PAPER

Microfracture propagation in gneiss through frost wedging: insights from an experimental study

Ferdinando Musso Piantelli[1] · Marco Herwegh[1] · Flavio S. Anselmetti[1,3] · Marius Waldvogel[1] · Ueli Gruner[2]

Abstract

Ice-driven mechanical weathering in mountainous environment is considered as an efficient process for slow but cyclical mechanical preconditioning of rockfall events. In this study, we simulate subcritical microfracture propagation under frost wedging conditions along pre-existing mechanical weaknesses of intact rock bridges with an innovative experimental approach. Two series of freeze–thaw experiments conducted in an environmental chamber were carried out to investigate and monitor the propagation of artificially induced fractures (AIF) in two twin gneiss samples. A displacement sensor recorded the sample's in situ deformation in an environmental chamber during the experiments. 3D X-ray CT scans, performed before and after the experiments, as well as thin sections showing the post-experiment state of the deformed samples allowed tracking and quantification of fracture propagation. Our results demonstrate that frost wedging propagated the AIFs 1.25 cm^2 and 3.5 cm^2 after 42 and 87 freeze–thaw cycles, respectively. The experiments show that volumetric expansion of water upon freezing, cooperating with volumetric thermal expansion and contraction of the anisotropic rock, plays a key role in fracture widening and propagation. Based on these results, this study proposes that: (1) frost wedging exploits intrinsic pre-existing mechanical anisotropies of the rock; (2) the fracturing process is not continuous but alternates between stages of fast propagation and more quiet stages of stress accumulation; and (3) downward migration of "wedging grains," stuck between the walls of the fracture, increases the tensile stress at the tip, widening and propagating the fractures with each freeze–thaw cycle. The experimental design developed in this study offers the chance to visualize and quantify the long-term efficiency of frost wedging in near-natural scenarios.

Keywords Frost wedging · Fracture propagation · Wedging grains · Rock bridges · Low-porosity jointed rocks

---

✉ Ferdinando Musso Piantelli
ferdinando.musso@geo.unibe.ch

Extended author information available on the last page of the article

 🌊 Springer

1 Introduction

Physical rock weathering is a crucial and hazardous process constantly active in mountainous environment. Under cold and humid climate, with frequent freeze–thaw cycles, ice-driven mechanical weathering is generally considered to be a critical process that affects rock slope stability. Recognition of the role that this phenomenon may play in preconditioning and triggering rockfalls and sediment production has drawn the attention of researchers for decades (Tricart 1956; Rapp 1960; Tharp 1987; Hallet 2006; Savi et al. 2015; Jia et al. 2017; Krähenbühl et al. 2018). Rock slope failure is mainly dominated by the complex interaction between existing natural mechanical discontinuities (e.g., bedding planes, foliations, joints, fractures, faults) and subcritical fracture propagation through intact rock bridges (Eberhardt et al. 2004; Kemeny 2005; Einstein et al. 1983). Rupturing of cohesive rock bridges is indeed considered one of the most important processes that controls rock mass failure followed by gravitationally driven collapse (Scavia and Castelli 1996; Kemeny 2005). In case of high-altitude mountainous terrain, the regular occurrence of ice at rock fall backscarps after a collapse of rock walls (e.g., Gruber and Haeberli 2007; Phillips et al. 2017) indicates that ice-driven mechanical weathering may be a critical factor that leads rock bridges to fail. A large number of field, experimental and theoretical studies addressed the mechanics of frost wedging (e.g., Tharp 1987; Jia et al. 2017; Weber et al. 2017); however, spatial and temporal controls of this process remain elusive (Hales and Roering 2007; Matsuoka 2001a; Hallet et al. 1991). Over the last 40 years, periglacial geomorphologists have identified two competing hypothetical processes responsible for frost weathering: volumetric expansion and ice segregation.

The volumetric expansion theory argues that when water completely fills pore space in the rock (total pore filling > 91 vol%), ice-induced expansion increases tensional stress at crack tips and leads to lengthening and widening of pre-existing pores or macro-/microfractures within the rock mass (e.g., Church et al. 1979; Hall and Thorn 2011). In contrast, the ice segregation theory claims that nanometer-scale water films (premelted films), existing between ice and the mineral surface, exert a "disjoining pressure" induced by van der Waals and electrostatic forces that tend to separate ice from the substrate (Walder and Hallet 1985; Hallet et al. 1991; Worster and Wettlaufer 1999; Hallet 2006). The ice segregation mechanism and associated disjoining forces are considered of being able to fracture the rock. However, volumetric expansion and ice segregation do not necessarily contradict each other and neither process in isolation is able to clarify exhaustively the rates, efficiency and mechanics of frost-induced degradation of rocks (Matsuoka 2001b). In addition, their spatial applicability and interaction with other important variables (e.g., host rock properties, thermally induced stresses) are even less known (Hall and Thorn 2011).

Many field studies have been conducted in low-porosity (< 5 vol%) fractured rocks, which compose the majority of the world's high mountain chains (Matsuoka 2001b; Weber et al. 2017). In addition, since frost weathering operates slowly in the field, laboratory simulations have been often used for comprehending the long-term evolution of this process. In literature, experimental studies that investigated these processes active in jointed low-porosity rocks are scarce (Davidson and Nye 1985; Jia et al. 2017; Matsuoka 1995), whereas most of the studies focused on intact rock samples with medium (5–20 vol%) to high porosity (> 20 vol%) (Matsuoka 2001b; Nicholson and Nicholson 2000). Furthermore, the experiments conducted in low-porosity rocks simulated frost wedging in part-through fractures, which were artificially induced by pre-experimental saw cuts. Their smooth cut

surface, as well as the resulting considerable gap between the cut walls, only approximates natural geometries necessary for fracture tip propagation in a simplified way.

The purpose of this study is to investigate microfracture propagation under frost wedging conditions that may affect cohesive intact rock bridges along low-porosity jointed rock slopes. To examine the long-term efficiency of this process, we simulated the propagation of artificially induced fractures (AIF) in gneiss with an innovative experimental approach. Through a series of experiments, we: (1) developed a new experimental design that facilitates an accurate characterization of the active process; (2) gained new insights into the exact fracture propagation mechanism; (3) illustrate how rock properties influence the fracture propagation allowing us to (4) bridge the gap that currently exists between field studies and laboratory simulations of frost wedging in low-porosity jointed rocks.

2 Experimental design

Our test specimens are two twin gneiss cylinders (GN_1 and GN_2), 2.5 cm diameter ('1-inch') and 5 cm in height (Fig. 1c), which have been drilled out alongside the foliation and parallel to the lineation of a former large intact gneiss block. The block derived from the Central Aare Granite (Berger et al. 2017; 46° 33′ 46″ N, 8° 20′ 18″ E) and represents a ductile deformed part of this granite (mylonites in Wehrens et al. 2016, 2017), which we refer for sake of simplicity in the following as "gneiss."

Samples GN_1 and GN_2 are characterized by a classic gneissic texture with granitic composition expressed in 35 vol% quartz, 35 vol% feldspar, 15 vol% biotite, 10 vol% chlorite, 5 vol% epidote. The foliation of the rock shows alternation of: (1) ~ 2-mm thick layers of quartz + feldspar + biotite (± chlorite) and (2) ~ 0.5-mm thick layers of ultra-fine polymineralic aggregates composed of epidote + chlorite + quartz. Up to 2-mm large relict quartz grains show ductile deformation in form of a combination of subgrain rotation recrystallization and subsequent annealing by grain-boundary migration recrystallization, resulting in an average grain size of ~ 150 μm (see Bambauer et al. 2009; Wehrens et al. 2016, 2017 for details). Pristine phenocrysts of feldspar, ~ 1 mm in size, are rotated, rounded at the edges and damaged by several microfractures. The cores of the phenocrysts are altered to fine-grained white mica (sericitization). The ~ 200 μm large biotite grains are preferentially oriented along the foliation of the rock. Chlorite grows pseudomorphically after biotite grains, in some cases replacing them completely. During the upper greenschist metamorphic conditions at the time of Alpine deformation, ultra-fine-grained polymineralic bands (quartz, epidote, biotite, white mica and albite) developed parallel to the main foliation in the host granite (see ultramylonites in Wehrens et al. 2016, 2017 for details). Each sample contains a tapered-shaped (Tharp 1987) artificially induced fracture (AIF). Artificial fracturing was performed using a hydraulic press by loading a wedge-shaped piston inserted in a pre-cut notch on the top surface of the gneiss cylinders (Fig. 1a, b). The 2-mm large and deep notches alongside the upper half of the cylinder (Fig. 1a, c), and two tight metallic rings, (placed around the sample at 1/3 and 2/3 of cylinder's height), helped to localize the fracture in the middle of the specimen along the foliation. and prevented disassembling of the sample by sideward fracture propagation (Fig. 1a, b). The shape and geometry of the AIFs differ from previous studies that used smooth saw cuts with pronounced apertures going entirely through the upper half of the sample (e.g., Davidson and Nye 1985; Jia et al. 2017). In our study, newly formed and propagated AIF with small
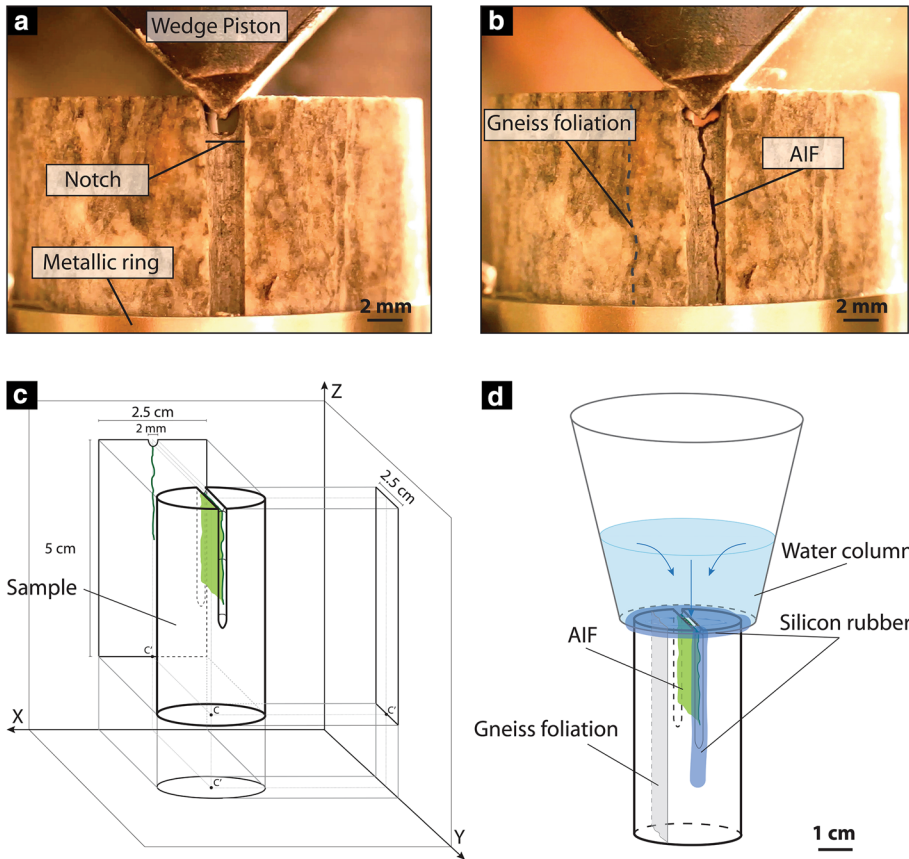
Fig. 1 Upper part of the gneiss sample GN_1 before (**a**) and after (**b**) the generation of the foliation parallel artificially induced fracture (AIF) after the wedge–piston has been loaded with a press. The 2-mm deep and wide notches on the lateral and top surface of the sample favoured the crack localization in the center of the sample. **c** 3D block diagram and relative dimensions of the specimen. **d** 3D representation of the sample setup before starting the freeze–thaw test

apertures (<500 μm) realistically simulate roughness and sinuosity as is the case in natural fractures.

Before and after any experimental series, the 3D spatial distribution of the AIF has been characterized by 3D X-ray computed tomography (CT) (Bruker Skyscan 2211—Multi-scale X-ray nano-CT system). 3D X-ray CT offers a non-destructive imaging solution to analyze the internal spatial structure of the samples with 15 μm voxel resolution. All the CT scans have been performed with fixed settings (X-ray source: 140 kV and 120 μA; source focus mode: high power; filter: 0.5-mm Mo), in order to allow comparisons of the fracture surface before and after the experiments. The obtained dataset (3D reconstructed with NRecon software (1.6.10.5)) was then loaded in the software Avizo (9.4.0) where, after image processing (interactive thresholding and manual image segmentation), the 3D fracture surface was visualized (see supplementary material in the Online Resource 1).

Before starting the experiments, the specimens were immersed for 30 min in water recreating natural saturation of the AIF. During the tests, a water column (40 ml, Fig. 1d)

on top of the samples provided constant water saturation inside of the fracture preventing evaporation processes. The sides of the AIF were sealed with silicone rubber to avoid lateral water leakage (Fig. 1d). The experiments were performed in an environmental chamber (Frost-Defrost Chamber Toropol Type K010/K012/K015) within a temperature range from $+20$ to -20 °C. A high-precision thermometer (Pt100-4L, range -100 to $+200$ °C (USB sensor interface 9206-V0002), 0.02 °C uncertainty, sampling frequency $= 0.1°$Hz) monitored the air temperature of the chamber in immediate proximity of the sample. In this study, we performed two main series of experiments: series I on sample GN_1, and series II on sample GN_2.

During series I, sample GN_1 has been investigated with X-ray CT scan over the course of the experiment and, once concluded, with optical microscopy on thin sections of the sample (30 μm thick, cut along the x–z plane (Fig. 1c). In this experiment series, GN_1 underwent 7 preliminary freeze–thaw cycles (temperature regimes indicated in Fig. 2a) with the frequency of 1 cycle a day. Subsequently, we programmed the environmental chamber to perform 80 additional freeze–thaw cycles (temperature regimes indicated in Fig. 2b) at the frequency of 4 cycles a day. At the end of the experiment, during the thin-section preparation procedure, sample GN_1 was placed in a mold and impregnated with EPOXY resin (EPO-TEK 301 ILB mixed with Fluorescein ($C_{20}H_{12}O_5$) to provide fluorescence properties) under vacuum conditions (1.5×10^{-2} Pa) allowing a complete impregnation of the fracture preserving the solid structure for polishing.

During series II, sample GN_2 was inserted in a tailor-made sample holder made up entirely of aluminum (Fig. 2d) that kept the gneiss cylinder fixed in the same position for the duration of the test. The sample holder was equipped with a displacement sensor (LVDT Displacement Sensor, IN-line amplifier, Model 8738 (USB sensor interface 9206-V0002), 0.0025 mm accuracy, sampling frequency $= 0.1°$Hz) positioned perpendicularly to the z-axis of the sample (Fig. 2e), monitoring constantly the variation of the cylinder's
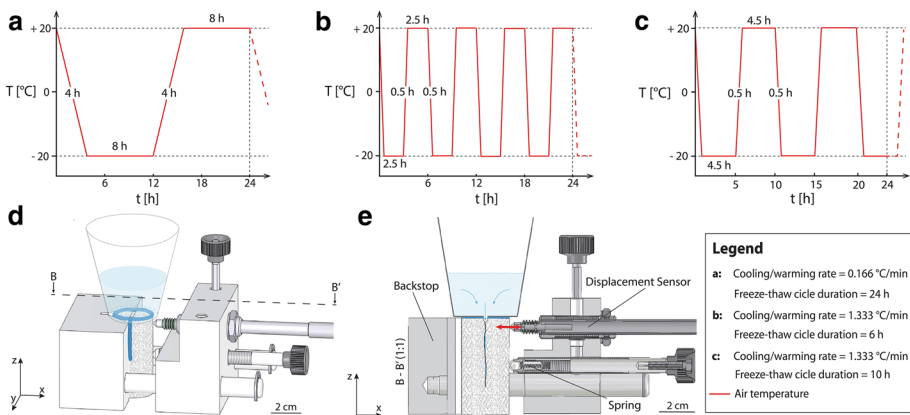
Fig. 2 a 24-h representation of the temperature regime employed during the 7 preliminary freeze–thaw cycles of series I. **b** 24-h representation of the temperature regime of the 80 additional freeze–thaw cycles of series II. **c** 24-h representation of the temperature regime of the 60 freeze–thaw cycles performed in series II. **d** 3D sketch of the experimental setup of series II GN_2 is inserted in the tailor-made sample holder that keeps the sample fixed for the entire duration of the test. **e** B–B′ cross section of the setup of series II, a soft spring ($k = 7.35$ N/m) keeps the sample attached to the backstop. The displacement sensor, positioned perpendicularly to the z-axis of the cylinder, measures the diameter variation (red arrows) during the tests

diameter. Before testing, a number of "dry tests" (on a third intact gneiss sample devoid of fracture and water) were conducted to characterize the thermal response of the material and determine the baseline parameters for calibrating the displacement sensor (see supporting information in the Online resource 2 for calibration of the sensor). The employed displacement sensor, at each $+20/-20$ °C transition, required 2 h to re-equilibrate at the new induced temperature conditions. Therefore, we were forced to extend the time spent at $+20$ and -20 °C to 4.5 h. During this test series, sample GN_2 underwent 69 freeze–thaw cycles (temperature regimes indicated in Fig. 2c) at the frequency of ~2.5 freeze–thaw cycles a day.

3 Results

The two series of experiments have been designed to characterize different features of freeze–thaw weathering occurring in our specimens. The first series investigated if and in which manner crack propagation occurs and, if so, how it is influenced by rock properties. The second series focused on monitoring the fracturing process active during the experiments. By combining the obtained results, we derive a reliable and complete simulation of the long-term efficiency of frost wedging in low-porosity jointed and active rock slopes.

3.1 Series I (sample GN_1)

Before starting the freeze–thaw experiment, sample GN_1 was scanned in the 3D X-ray CT (Fig. 3a). The AIF in the sample displayed a classic tapered shape, where the aperture diminishes gradually from the top (aperture ~250 μm) toward the tip (few μm) (Fig. 3b, c). The fracture is ~3.8 cm long and mainly follows the foliation, except the central section, where it branches off in two parts. The first branch proceeded along the foliation, whereas the second branch departed perpendicularly to the latter stopping ~1 mm before reaching the sample's side surface (Fig. 3c).

During the first part of this experimental series, GN_1 underwent 7 freeze–thaw cycles (temperature regimes indicated in Fig. 2a). The goal of this preliminary test was to provide a quantitative estimate of the number of freeze–thaw cycles required to
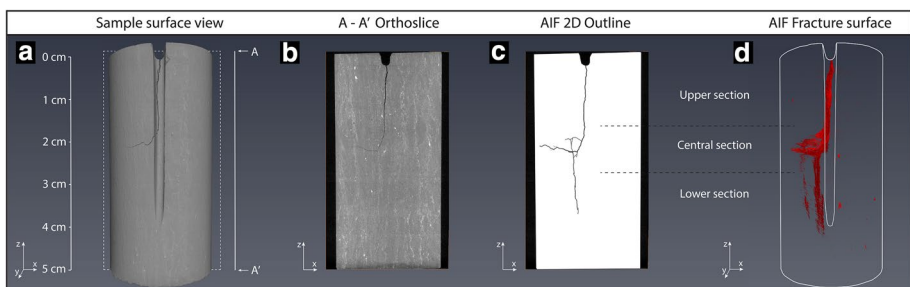
Fig. 3 X-ray tomographic images: **a** 3D surface view of sample GN_1. **b** A–A′ orthoslice along the x–z plane through the sample, dark shades correspond to low-density components (e.g., fractures), whereas lighter shades correspond to high-density materials. **c** Thresholded two-dimensional outline of the AIF in A–A′ orthoslice excluding the background image. **d** 3D surface visualization of the AIF (red) contained in sample GN_1

simulate long-term fracture propagation. A second CT scan was performed after this first part of the test. By comparing the two fracture surfaces, before and after the experiments, no relevant changes were observed, requiring the sample to be subjected to a substantially enhanced number of freeze–thaw cycles.

Consequently, the environmental chamber has been programmed to perform 80 additional freeze–thaw cycles (temperature regimes indicated in Fig. 2b). At the end of the 87 cycles in total, a third CT scan was performed (Fig. 4a). By overlapping and comparing the fracture surfaces at the beginning of the series and after 87 cycles (red and light blue surface in Fig. 4a–c, respectively), the following observations were made:

1. In the lower section, the AIF fracture propagated (PF) ~ 1 cm down in the sample (Compare Figs. 3d and 4a).
2. In the lower section, the two originally separated sides of the AIF along the gneiss foliation were patched in a unique corrugated fracture surface (Fig. 4b, c).
3. The central branch of the AIF, which proceeded perpendicularly to the foliation, did not propagate during freeze–thaw cycles although only 1 mm was missing to achieve lateral sample failure.
4. Overall, the newly formed PF extended the fracture surface by 3.5 cm^2.

When the freeze–thaw experiment was completed, thin sections of the sample, cut along the x–z plane (Fig. 1c), were examined with light optical microscopy. The analysis revealed that the AIF propagated for 3.8 cm into the sample and stopped when it encountered a ~ 1-mm large fractured feldspar porphyroclast (Fig. 5b). During subsequent freeze–thaw cycling, the PF propagated rigorously along the main pre-existing natural weaknesses of the rock: (a) along cleavage and grain boundaries of preferentially oriented biotite/chlorite grains (Fig. 5c); (b) along the ultra-fine polymineralic aggregates layers (Figs. 5b, d); and (c) along grain boundaries (Fig. 5b). The PF propagated with an aperture of ~ 15–20 μm avoiding propagation through feldspar and quartz grains. Every time that one of these minerals was encountered by the PF, further fracture propagation was blocked and had to deviate to the nearest pre-existing rock weakness (Fig. 5b, d).
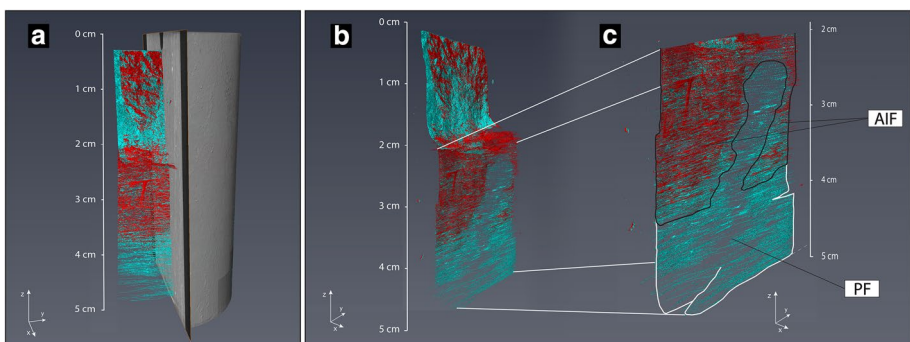

Fig. 4 X-ray tomography images. **a** Right side sample half-cylinder with the detected 3D fracture surface in the excluded left-side part (sample GN_1 after 87 freeze–thaw cycles). **b** 3D Visualization of both the AIF surface (red) and the propagated fracture (PF) after 87 cycles (light blue). **c** Close-up of the lower section of the fracture: the two originally separated sides of the AIF have virtually been patched together showing that the fracture tip moved 1 cm down toward the sample's bottom
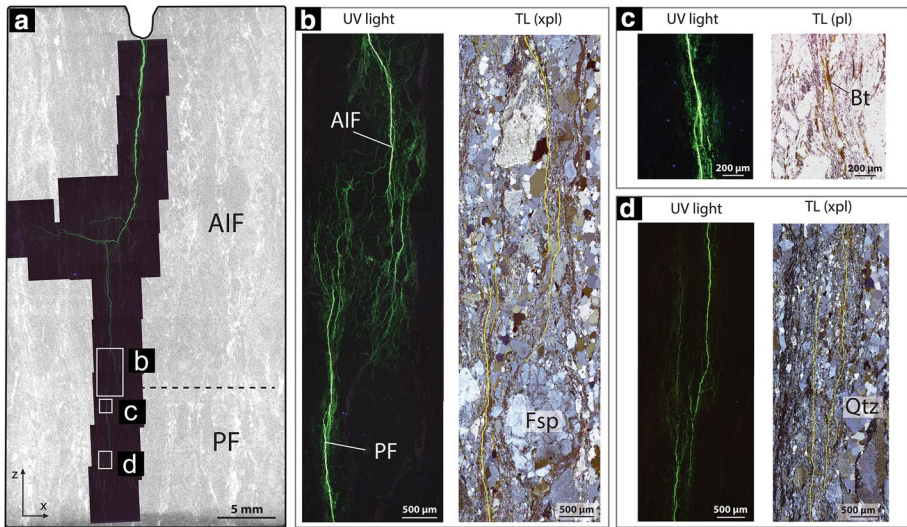
Fig. 5 a Overview of the fracture of sample GN_1 in thin section under UV light. As background *X–Z* orthoslice visualization in the same position of the post-experiment thin section. **b** UV light and transmitted light [crossed polarized light (xpl)] micro-photograph of the transition between the AIF and the PF (area b in plate **a**). The AIF stopped encountering a 1-mm large fractured feldspar porphyroclast (TL). To proceed, the PF had to deviate to the neighboring ultra-fine polymineralic aggregate layer (TL and UV). **c** UV light and transmitted light (plane polarized light (pl)) micro-photograph showing PF propagation along the cleavage of preferentially oriented biotite grains (area c in plate **a**) (TL). **d** UV light and transmitted light (xpl) micro-photograph showing a bridging of the PF path from an ultra-fine polymineralic aggregate layer to a neighboring one (area d in plate **a**)

3.2 Series II (sample GN_2)

Using a displacement sensor, we aimed in the second test series to monitor fracture propagation until sample failure. In order to achieve this, a longer AIF was induced within sample GN_2. The standard 3D CT scan before starting the experiment reveals the fracture surface (Fig. 6). Since the applied pressure in the hydraulic press to generate a longer AIF was greater than the one applied for GN_1, two conjugated AIFs formed in addition to a
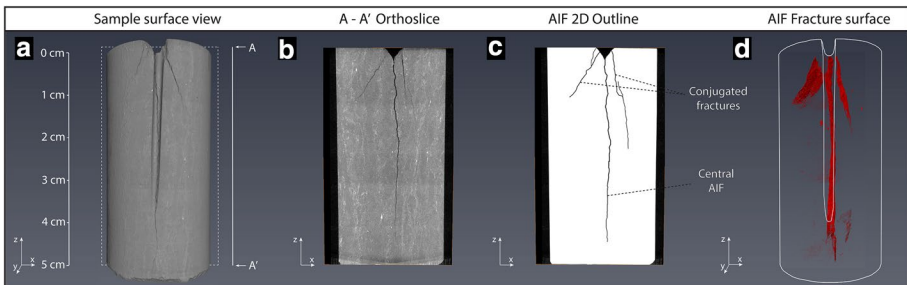

Fig. 6 X-ray computer tomography images: **a** 3D volume rendering of sample GN_2. **b** A–A′ orthoslice along the *x*–*z* plane through sample GN_2. **c** Two-dimensional outline of the AIFs: at the side of the central main AIF, the two conjugated AIFs are visible. **d** AIF 3D surface visualization of sample GN_2

central main AIF at its sides (Fig. 6c). Because we intended to observe the propagation of the central AIF only, we sealed the top of both conjugated AIFs avoiding water infiltration at these sites. The central AIF was ~4.5 cm long, missing 5 mm to complete failure and exhibited a tapered shape as in sample GN_1, with an aperture (~300 μm at the top) that diminishes gradually toward the fracture tip (few μm) (Fig. 6b, c).

Before testing sample GN_2, a "dry test" was conducted on a third intact gneiss sample devoid of fractures and water to characterize the thermal response of the host material (Fig. 7a). At each −20 °C interval during this test, the displacement sensor recorded in
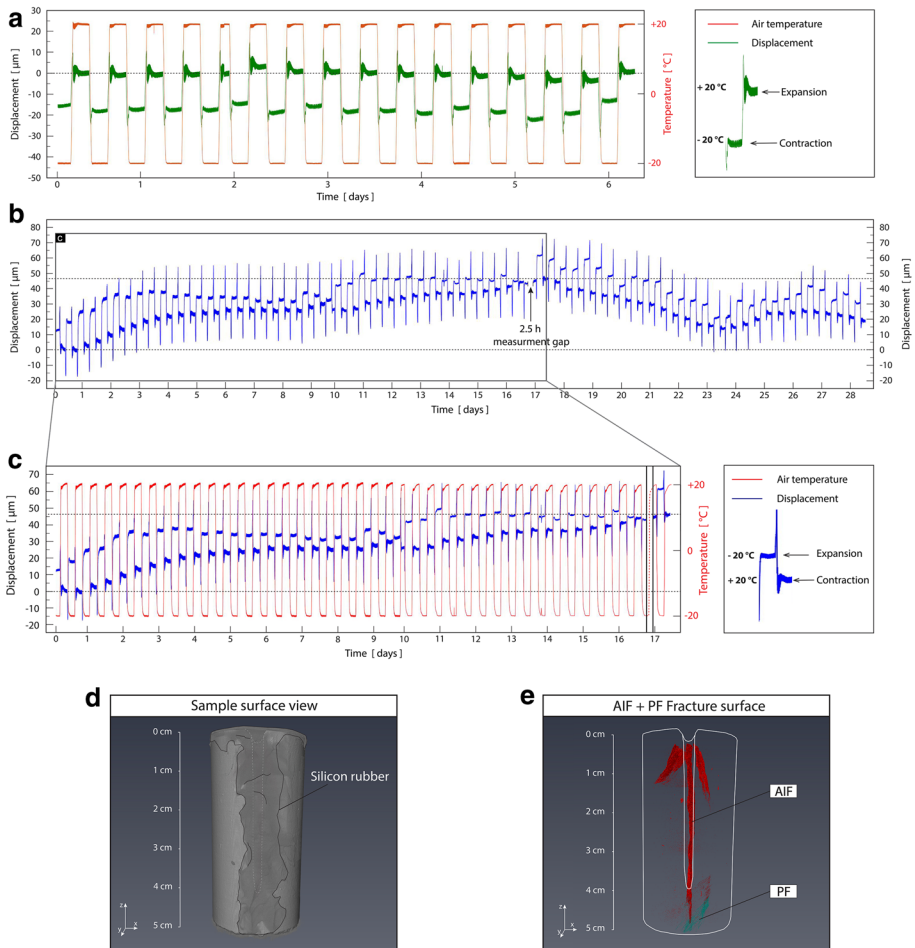
Fig. 7 Displacement records and X-ray tomography images. **a** Temporal variation in sample diameter width (green curve) and air temperature in the chamber (red curve) during the "dry test". Note that the gneiss cylinder experienced a volumetric thermal contraction and expansion, respectively, at 0 to −20 °C and 0 to +20 °C. **b** Temporal variation in sample's GN_2 diameter width (blue curve) during test series II. **c** Close-up of **b** during the first 17.5 testing days of series II. **d** 3D surface of sample GN_2 at the end of series II. The silicon rubber, still in place, seals the sides of the crack. **e** 3D view of both the AIF surface (red) and of the propagated fracture (PF) at the end of the experiment (light blue). PF reached the bottom of the sample but the silicon rubber still holds the two parts of the specimen together

average a 16 μm contraction of the sample diameter. At each +20 °C interval, the diameter of the sample returned to the initial value measured at the beginning of the experiment (tared to 0.000 mm at +20 °C) (Fig. 7a).

GN_2 experienced 69 freeze–thaw cycles with temperature regimes indicated in Fig. 2c. At the beginning of the test, the measured value of the diameter of the cylinder at +20 °C was tared to 0.000 mm. On the 16th day, a pause of 2.5 h occurred in the displacement measurement (Fig. 7b). During this pause, only the data recording of the displacement sensor was stopped for downloading the recorded dataset, while the cooling/heating cycles in the chamber continued. Once the +20 °C temperature conditions in the chamber were reached again in the next cycle, data recording of the displacement sensor was restarted, which had to arbitrarily be tared to the diameter dimensions recorded at the last +20 °C interval. Because of this procedure, the uncertainty of the absolute diameter amounts to a maximum of 22 μm. The obtained results (see Fig. 7b for the complete deformation record acquired during the test) can be summarized in the following way:

1. At each −20 °C interval, the displacement sensor recorded a variable expansion of the sample's diameter ranging between 22.5 μm and few μm (~12 μm average). At each +20 interval, the sensor recorded a contraction.
2. Within the first 17.5 days of testing (42 freeze–thaw cycles), the diameter of the sample increased by ~46 μm.
3. Between the 18th and the 23rd day (between the 43rd and 57th freeze–thaw cycles), the former total length change of the sample's diameter dropped to 14 μm.
4. In the final days of the test (58th to 69th freeze–thaw cycles), the total length of the sample's diameter increased again to 25 μm, decreasing then to a final value of 18 μm.

At the end of the test, a second CT scan on sample GN_2 was performed with the crack still sealed by the silicon rubber (Fig. 7d). The CT scan reveals that the specimen entirely broke through by the PF (Fig. 7e), but the remaining silicon rubber at the cylinder's side kept the two parts together. To reach the bottom of the sample, the PF propagated for ~0.5 cm extending the fracture surface by ~1.25 cm^2.

4 Discussion

The results obtained from the two series of experiments provide crucial insights into multiple features of frost wedging active in the tested specimens. In this section, we first provide a discussion of the deformation record acquired during test series II. Then, the discussion integrates microstructural observations on thin sections, derived from sample GN_1, providing a complete characterization of the investigated fracture propagation processes.

The dry test conducted in the sample devoid of fractures and water showed that over the temperature range from +20 to −20 °C ($\Delta T = 40$ K) the gneiss experienced a regular thermo-elastic oscillation of ~16 μm (peak-to-peak amplitude; Fig. 8a). At each −20 °C interval, the cylinder experienced a linear thermal contraction of ~16 μm (Fig. 8c) and an equivalent linear thermal expansion at each +20 °C interval.

During test series II, sample GN_2 experienced an opposite behavior, as a variable expansion (~12 μm average) has been observed at each −20 °C interval and a contraction at each +20 °C interval. The recorded expansion at −20 °C is attributed to the volumetric expansion of the water contained in the fracture upon freezing (9 vol% Tharp 1987). The
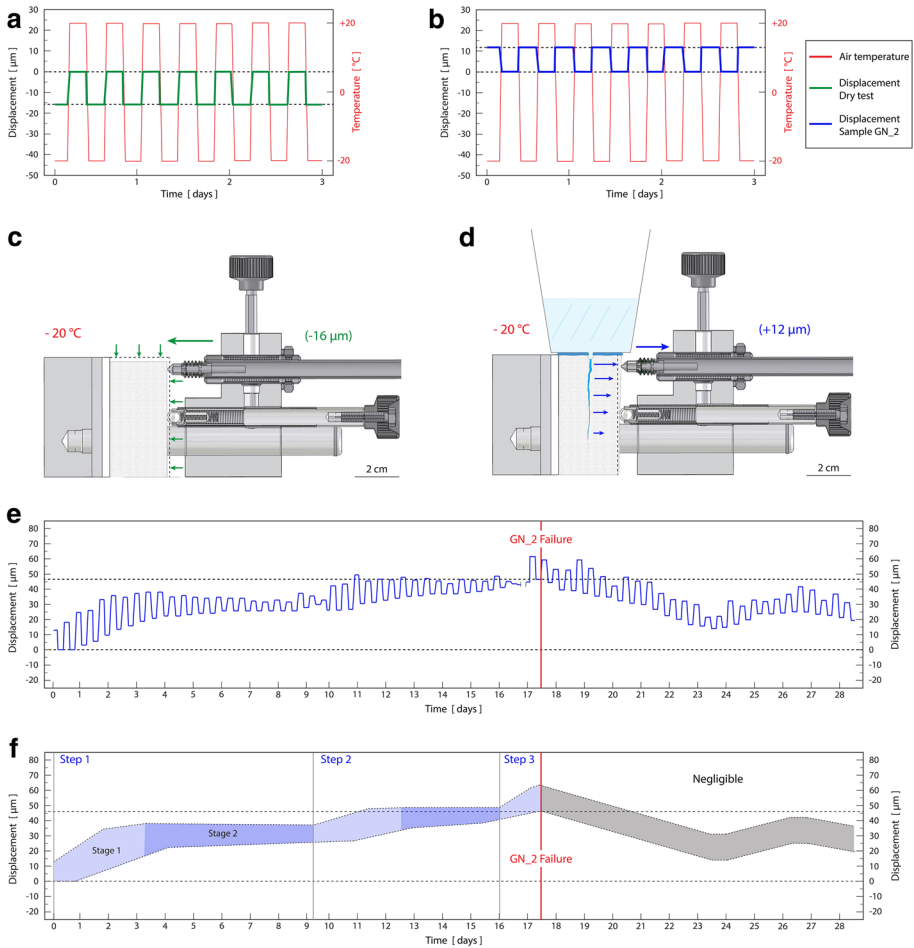
Fig. 8 **a** Schematic representation of three days long the temporal variation in sample diameter width (green curve) and air temperature in the chamber (red curve) during the "dry test." **b** Theoretical temporal variation in sample's GN_2 diameter width, in absence of irreversible deformation, (blue curve) and air temperature in the chamber (red curve) during the test series II. **c** Cross section along the experimental setup during the "dry test" at −20 °C. The displacement sensor records the −16 μm thermal contraction (green arrows) of the gneiss sample. **d** Cross section along the experimental setup during test series II at −20 °C. The displacement sensor records +12 μm fracture widening induced by the volumetric expansion of water upon freezing (blue arrows). **e** Simplified representation of the temporal variation in sample's GN_2 diameter width (blue curve) during the test series II. **f** Interpretation of the deformation trend (light blue field) recorded during test series II. The first 17.5 days are divided in three steps and each of them is subdivided in two stages. After the sample failure that occurred at 17.5 days, deformation trend (gray field) is considered negligible

cryostatic pressure resulted in fracture's aperture widening and consequently in diametrical expansion of the cylinder as sketched in Fig. 8d. Above 0 °C, water thawing reduces again the volume and induces a closure of the fracture recorded as a diametrical contraction.

Despite the observation of an opposite trend with respect to the one described during the dry test, the intrinsic thermo-elastic oscillation characteristic of the material is still

present and operates simultaneously. Therefore, at −20 °C, the volumetric expansion of water upon freezing counteracts and overcomes the thermal contraction of gneiss since it is almost twice as large as the latter [Fig. 8b, ~28 μm of linear expansion recorded by the extensometer (16 + 12 μm)]. In addition, we infer that ice extrusion processes (Davidson and Nye 1985) did not reduce the effect of ice volumetric expansion since the extrusion is strongly inhibited by roughness and sinuosity of the fracture that provides a large contact area between ice and rock. This interpretation is confirmed by the fact that the fracture, initially ~300 μm wide, was widened by 28 μm at −20 °C, a value that can be directly related to the theoretical 9% volumetric expansion of water under freezing condition (Tharp 1987).

In presence of only reversible deformation processes, a standard time series of fracture widening and closing should be recorded as represented in Fig. 8b. Any shift from this standard time series has to be related to non-elastic and therefore irreversible deformation processes. In the displacement record acquired during the test series II (Fig. 8e), fracture widening (at −20 °C intervals) and closing (at +20 °C) are clearly observable but not constant and the specimen diameter at +20 °C changes through time. At the end of series II, the CT scan revealed that the PF in sample GN_2 propagated by ~0.5 cm reaching the bottom of the sample and extending the fracture surface by ~ 1.25 cm². The gradual increase of ~46 μm of the specimen's diameter, recorded within the first 17.5 days of testing (42 freeze–thaw cycles), is interpreted to correspond to the fracture propagation process that led to complete failure of the sample (with an average fracture propagation rate of 119 μm per cycle). This interpretation is consistent with what has been observed in series I, where the PF of sample GN_1 needed 87 freeze–thaw cycles to propagate for 1 cm down in the sample, reflecting an average fracture propagation rate of 115 μm per cycle.

Once sample GN_2 failed, the deformation is no more controlled by the specimen's physical properties but as artificially affected by the holding spring on the sample's side (Fig. 2e). The subsequent abrupt drop between the 18th and the 23rd day (Fig. 8e) is therefore related to partial closure of the fracture induced by the spring immediately after the failure. In the final days of the test, the data indicate a non-systematic opening and closing of the fracture, which are interpreted as movements not anymore controlled by a connecting elastic hinge at the base of the sample but rather by the two separate cylinder halves pressed together by the spring during the final freeze–thaw cycles. Consequently, for the purpose of this study, the period after 17.5 days of testing is not considered.

The deformation curve acquired in the first 17.5 testing days shows a gradual increase of the sample's diameter articulated in three steps. At the end of the third step, sample failure occurred as just mentioned (Fig. 8e, f). The deformation trend of the three steps displays a characteristic and repetitive shape with two stages, which are discussed in detail for the first step (Fig. 8f):

(Stage 1) At the beginning of the step, the fracture's aperture increases simultaneously both at −20 °C and at +20 °C. This interval is interpreted as a first phase of fracture propagation, as during −20 °C intervals, ice-induced expansion increases tensional stress at crack tips leading to a lengthening and widening of the AIF. During +20 °C intervals, the sample's diameter does not return to its previous values and slightly increases so that more water can migrate further into the newly formed PF. Consequently, alternating freeze–thaw cycles lead to fracture propagation

(Stage 2) After 8 freeze–thaw cycles (3 days), the fracture's aperture during −20 °C intervals approaches a stable value, whereas aperture during +20 °C intervals

firstly increases at the same rate of the first stage gradually reaching then a stable value as well. This second stage is interpreted as a halt in fracture propagation and tensile stress accumulation at the fracture tip. This second stage lasts until the accumulated tensile stress is large enough to overcome the rock strength initializing a new step and further propagating the fracture

The record supports the assumption that fracture propagation occurs in response to stresses induced by volumetric expansion of water upon freezing. In addition, this behavior also demonstrates that the fracture propagation process is rate-sensitive, i.e., not continuous since it responds to discontinuous tensile stress accumulation, likely related to heterogeneities in the sample's microstructure. Observations through light optical microscopy, performed on sample GN_1, revealed that polymineralic bands and aligned phyllosilicates (biotite, chlorite, white mica), form the major microstructural anisotropies of the samples crucial for microfracture propagation (Fig. 5b, d and c). In addition, the propagation processes are related to continuous and relatively rapid stages in fracture propagation along the pre-existing weaknesses of the rock (Stage 1, Fig. 8f). In the case of rigid obstacles, however, a stop in fracture propagation yields in the local accumulation of tensile stresses until reaching the yield strength of the obstacle's interface with the rock matrix, allowing further propagation of the microfracture along the obstacle grain boundaries (Stage 2, Fig. 8f). This microstructural heterogeneity (quartz and feldspar clasts) and associated local stress perturbations slow down fracture propagation.

4.1 Supportive role of "wedging grains"

Observations of the thin section of sample GN_1 indicate the critical role of 200–300 μm large fractured quartz, feldspar and biotite fragments that become stuck between the fracture walls. Comparison of the CT orthoslices of the scans performed at the beginning and at the end of the tests indicates that these grains were not fixed to the fracture walls but they changed their position by successively falling down into the fracture with progressive freeze–thaw cycling. As an example, two grains identified after 87 freeze–thaw cycles in the upper section of the AIF (Fig. 9e) were not present at this location at the beginning of the experiment (Fig. 9a–d). By a gravity-driven downward migration of these grains during unfrozen conditions, they act as a natural wedge (hence named as "wedging grains") blocking the fracture from further closing upon thawing. Owing to the wider fracture aperture at the onset of the next freezing stage, more water is present in the fracture, rising the tensile stress component and forcing the microfracture to propagate further. These wedging grains therefore strongly support the crack propagation process. The five simplified sketches in Fig. 10 show how the migration of wedging grains induces an irreversible increase of the fracture width (+20 °C) during a tensile stress accumulation phase:

1. The central and the lower section of a tapered shape fracture, filled with water and a wedging grain stuck between the fracture walls (Fig. 10a).
2. At −20 °C, the volumetric expansion of the frozen water widens the fracture. The grain, which at −20 °C undergoes a volumetric thermal contraction, is surrounded by ice and is detached from the fracture walls (Fig. 10b, d).
3. During the warming phase slightly above 0 °C, the ice starts to melt from the fracture walls and from the water column above the sample. Consequently, the melting ice fringe retreats from a deeper position of the fracture, where the ice wedge is thinner, toward a
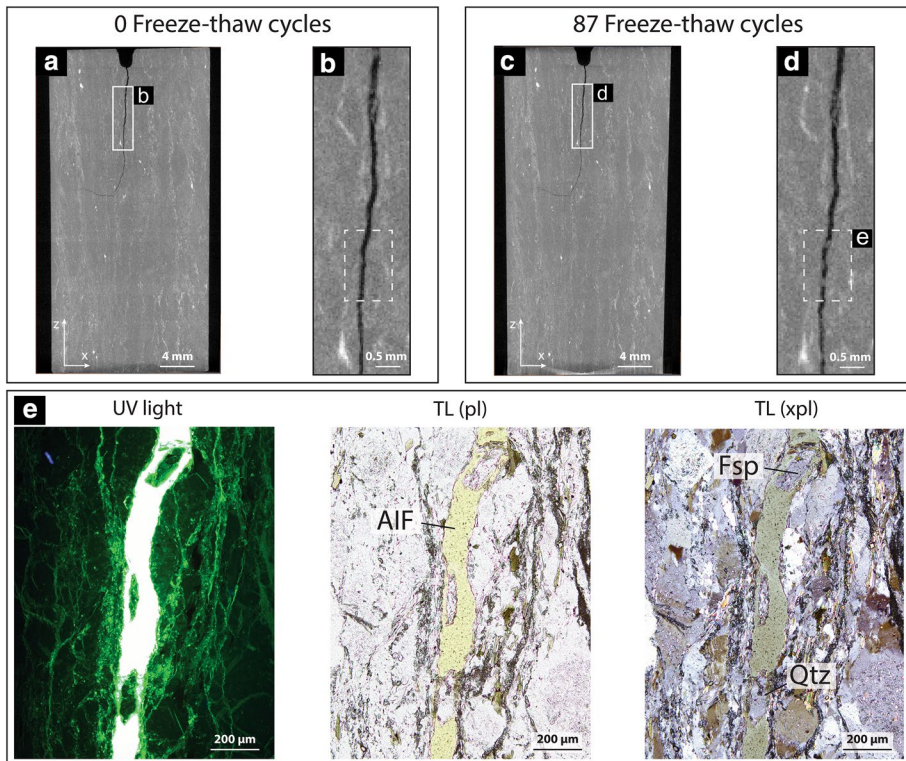
Fig. 9 *X–Y* orthoslice visualizations, in the same position of the post-mortem thin section (e, f), of the scanned GN_1 sample at **a** the beginning of test series I and **c** at the end of test series I, after 87 freeze–thaw cycles. **b**, **d** Close-up of the orthoslice along the upper section of the AIF before and after the 87 cycles, respectively. Note in dashed box in **d** appearance of rock fragments in the AIF which were absent at the beginning of the experiment (**b**). **e** UV light and transmitted light (pl and xpl) micro-photograph showing the two grains (feldspar and quartz) individuated with the CT stuck between the AIF walls (area e in fig. d)

    higher section, where the ice is thicker and thus requires more time to melt, still keeping the fracture open. As soon as the ice surrounding the wedging grain melts, the grain, possibly rotating, falls down into the fracture and becomes stuck between the fracture walls again (Fig. 10f).

4. Once +20 °C is reached, the fracture closes but the wedging grain that moved to a deeper section of the fracture impedes the complete closure, thus keeping the fracture open and widened permanently (Fig. 10c).

In the case of a tensile accumulation stage (Fig. 8f; Stage 2), more water can migrate in the fracture widened by the wedging grain, but the ice-induced volumetric expansion at −20 °C is not able to widen the fracture more than the previous cycle (Fig. 10d). However, as described previously (Fig. 10f), the grain can still fall deeper into the fracture and widen it more (Fig. 10e). On the contrary, in the case of a fracture propagation stage (Fig. 8f; Stage 1), the larger volume of water that migrated in the newly formed PF is able to widen
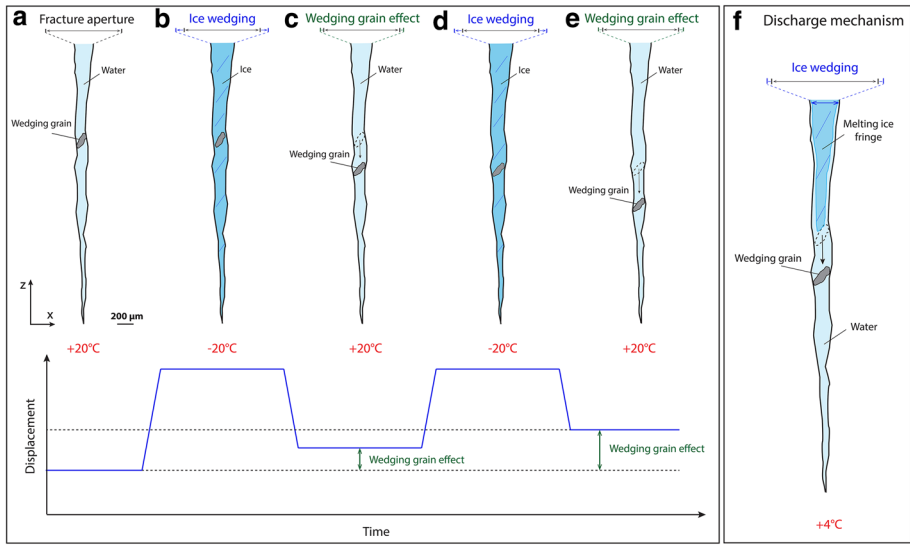
Fig. 10 Schematic drawings showing evolution of crack behavior during freeze–thaw cycles and the role of wedging grains. **a** Taper-shaped fracture at +20 °C filled with water and a wedging grain stuck between the fracture walls. Displacement–time diagram (bottom) represents the corresponding fracture aperture as recorded by the displacement sensor. **b** Fracture at −20 °C widened by the ice volumetric expansion and a grain detached from the fracture walls. **c** Fracture at +20 °C, the wedging grain moved to a deeper section of the fracture. As recorded by the displacement sensor, the wedging grain impedes the complete closure of the fracture. **d** Fracture again at −20 °C, the volumetric expansion of ice is not able to widen the fracture more that in stage b because of the high rock strength. Nevertheless, the wedging grain is again detached from the fracture walls. **e** Fracture at +20 °C, the wedging grain moved again to a deeper position in the fracture. As recorded by the displacement sensor, the wedging grain impedes the complete fracture closure inducing a larger permanent deformation that the one induced in stage c. **f** Simplified sketch of the discharge mechanism of the wedging grains slightly above 0 °C (here indicatively reported at +4 °C). The persisting top plug of the melting ice fringe still keeps the fracture widened and as soon as it releases the grain, the latter falls down in the fracture

the fracture upon freezing, causing easier downward migration of the wedging grains and allowing fracture propagation.

Downward migration of wedging grains is discussed here at the microscopic scale; nevertheless, we propose that this process also critically acts for fracture propagation under frost wedging conditions at larger scales with grains migrating in cm to m scale fractures.

5 Conclusions

This carefully monitored and characterized series of experiments sheds new light on the long-term efficiency of frost wedging operating in low-porosity jointed active rock slopes. By combining the obtained results, the following conclusions can be drawn:

1. Frost wedging is an efficient process that may propagate a fracture. The fracture of sample GN_2 increased its surface area after 42 freeze–thaw cycles by ~ 1.25 cm^2 (average fracture propagation rate of 119 μm per cycle). The fracture surface of sample GN_1

increased by ~3.5 cm^2 after 87 freeze–thaw cycles (average fracture propagation rate of 115 µm per cycle).

2. Volumetric expansion of water upon freezing, cooperating with volumetric thermal contraction and expansion of the rock, plays a key role in fracture widening and propagation.

3. The fracture propagation process under frost wedging conditions exploits intrinsic pre-existing mechanical weaknesses of the rock. The fracture propagation process is not continuous but occurs in an alternating manner reflecting successive stages of tensile stress accumulation. The alternations of these two stages are determined by the textural and mineralogical characteristics and heterogeneity of the rock such as grain or cleavage boundaries or polymineralic aggregates layers.

4. Migration of wedging grains toward the deeper sections of the fracture plays an important role in increasing the tensile stress at the fracture tip, eventually widening and propagating the fracture. The application of the wedging grains concept, here documented at the microscopic scale, can be extended to the interpretation of fracture propagation processes at larger scales (cm, m).

Ice-driven mechanical weathering, therefore, has to be taken into account as an active phenomenon that leads to subcritical fracture propagation through pre-existing weaknesses of intact rock bridges. In a rock wall, independently from the extent of the joints, fracture propagation under frost wedging conditions must initiate at the fractures tips and therefore operate at the microscale. The experimental design developed in this study replicates microfracture propagation occurring at the tip of natural joints visualizing the long-term efficiency of this process in near-natural scenarios. Consequently, the microfracture propagation process that has been documented in sample GN_1 and GN_2 does not aim to illustrate the exploiting of natural joints along the entire rock cliff, but describes the crucial process of fracture propagation initialized at the tips, a critical process that will eventually lead to destabilizing an entire rock slope.

Further systematic experimental studies are, however, required to elucidate frost wedging in low-permeability jointed rocks. In particular, future experiments should target to: (1) extend this experimental study to other rock types; (2) investigate the role of ice segregation by employing lower freezing rates during the freeze–thaw tests; and (3) calibrate the experimental results to natural systems evolving in this way a potential predictive tool for rock slope failure.

References

Bambauer HU, Herwegh M, Kroll H (2009) Quartz as indicator mineral in the Central Swiss Alps: the quartz recrystallization isograd in the rock series of the northern Aar massif. Swiss J Geosci 102(2):345–351

Berger A, Wehrens P, Lanari P, Zwingmann H, Herwegh M (2017) Microstructures, mineral chemistry and geochronology of white micas along a retrograde evolution: an example from the Aar massif (Central Alps, Switzerland). Tectonophysics 721:179–195

Church M, Stock RF, Ryder JM (1979) Contemporary sedimentary environments on Baffin Island, N. W. T., Canada: debris slope accumulations. Arct Alp Res 11(4):371–401

Davidson GP, Nye JF (1985) A photoelastic study of ice pressure in rock cracks. Cold Reg Sci Technol 11(2):141–153

Eberhardt E, Stead D, Coggan JS (2004) Numerical analysis of initiation and progressive failure in natural rock slopes—the 1991 Randa rockslide. Int J Rock Mech Min Sci 41(1):69–87

Einstein HH, Veneziano D, Baecher GB, O'reilly KJ (1983) The effect of discontinuity persistence on rock slope stability. Int J Rock Mech Min Sci Geomech Abstr 20(5):227–236

Gruber S, Haeberli W (2007) Permafrost in steep bedrock slopes and its temperature-related destabilization following climate change. J Geophys Res Earth Surf 112:148–227. https://doi.org/10.1029/2006JF000547

Hales TC, Roering JJ (2007) Climatic controls on frost cracking and implications for the evolution of bedrock landscapes. J Geophys Res Earth Surf 112:F02033. https://doi.org/10.1029/2006JF000616

Hall K, Thorn C (2011) The historical legacy of spatial scales in freeze–thaw weathering: misrepresentation and resulting misdirection. Geomorphology 130(1–2):83–90

Hallet B (2006) Why do freezing rocks break? Science 314(5802):1092–1093

Hallet B, Walder JS, Stubbs CW (1991) Weathering by segregation ice growth in microcracks at sustained subzero temperatures: verification from an experimental study using acoustic emissions. Permafrost Periglac Process 2(4):283–300

Jia H, Leith K, Krautblatter M (2017) Path-dependent frost-wedging experiments in fractured, low-permeability granite. Permafrost Periglac Process 28(4):698–709

Kemeny J (2005) Time-dependent drift degradation due to the progressive failure of rock bridges along discontinuities. Int J Rock Mech Min Sci 42(1):35–46

Krähenbühl R, Nänni C, Donauet F (2018) Prozesse die zu grossen Fels- und Bergsturz führen. Swiss Bull 23(1):29–56

Matsuoka N (1995) A laboratory simulation on freezing expansion of a fractured rock: preliminary data. Annual report of the Institute of Geoscience, The University of Tsukuba, vol 21, pp 5–8

Matsuoka N (2001a) Direct observation of frost wedging in alpine bedrock. Earth Surf Process Landf 26(6):601–614

Matsuoka N (2001b) Microgelivation versus macrogelivation: towards bridging the gap between laboratory and field frost weathering. Permafrost Periglac Process 12(3):299–313

Nicholson DT, Nicholson FH (2000) Physical deterioration of sedimentary rocks subjected to experimental freeze–thaw weathering. Earth Surf Proc Land 25(12):1295–1307

Phillips M, Wolter A, Lüthi R, Amann F, Kenner R, Bühler Y (2017) Rock slope failure in a recently deglaciated permafrost rock wall at Piz Kesch (Eastern Swiss Alps), February 2014. Earth Surf Proc Land 42(3):426–438

Rapp A (1960) Recent development of mountain slopes in Kärkevagge and surroundings, northern Scandinavia. Geogr Ann 42(2–3):65–200

Savi S, Delunel R, Schlunegger F (2015) Efficiency of frost-cracking processes through space and time: an example from the eastern Italian Alps. Geomorphology 232:248–260

Scavia C, Castelli M (1996) Analysis of the propagation of natural discontinuities in rock bridges. In: ISRM international symposium-EUROCK 96. International Society for Rock Mechanics and Rock Engineering

Tharp TM (1987) Conditions for crack propagation by frost wedging. Geol Soc Am Bull 99(1):94–102

Tricart J (1956) Etude expérimentale du problème de la gélivation. Biuletyn Peryglacjalny 4:285–317

Walder J, Hallet B (1985) A theoretical model of the fracture of rock during freezing. Geol Soc Am Bull 96(3):336–346

Weber S, Beutel J, Faillettaz J, Hasler A, Krautblatter M, Vieli A (2017) Quantifying irreversible movement in steep, fractured bedrock permafrost on Matterhorn (CH). Cryosphere 11(1):567–583

Wehrens P, Berger A, Peters M, Spillmann T, Herwegh M (2016) Deformation at the frictional-viscous transition: Evidence for cycles of fluid-assisted embrittlement and ductile deformation in the granitoid crust. Tectonophysics 693:66–84

Wehrens P, Baumberger R, Berger A, Herwegh M (2017) How is strain localized in a meta-granitoid, mid-crustal basement section? Spatial distribution of deformation in the central Aar massif (Switzerland). J Struct Geol 94:47–67

Worster MG, Wettlaufer JS (1999) The fluid mechanics of premelted liquid films. In: Shyy W, Narayanan R (eds) Fluid dynamics at interfaces. Cambridge University Press, Cambridge, pp 339–351

Affiliations

Ferdinando Musso Piantelli[1] · Marco Herwegh[1] · Flavio S. Anselmetti[1,3] · Marius Waldvogel[1] · Ueli Gruner[2]

[1]   Institute of Geological Sciences, University of Bern, Baltzerstrasse 1+3, 3012 Bern, Switzerland

[2]   Kellerhals und Häfeli AG, Kapellenstrasse 22, 3011 Bern, Switzerland

[3]   Oeschger Centre for Climate Change Research, Bern, Switzerland